JVST B
Journal of Vacuum Science & Technology B

Role of dose optimization in Ru atomic layer deposition for low resistivity films F

Cite as: J. Vac. Sci. Technol. B **41**, 012201 (2023); https://doi.org/10.1116/6.0002153
Submitted: 12 August 2022 • Accepted: 01 November 2022 • Published Online: 13 December 2022

Victor Wang, Michael Breeden, Nickolas Ashburn, et al.

COLLECTIONS

F This paper was selected as Featured

View Online Export Citation CrossMark

JVST B
Journal of Vacuum Science & Technology B
ARTICLE
avs.scitation.org/journal/jvb

Role of dose optimization in Ru atomic layer deposition for low resistivity films

Cite as: J. Vac. Sci. Technol. B **41**, 012201 (2023); doi: 10.1116/6.0002153
Submitted: 12 August 2022 · Accepted: 1 November 2022 ·
Published Online: 13 December 2022

View Online Export Citation CrossMark

Victor Wang,[1,a] Michael Breeden,[1] Nickolas Ashburn,[2] Matthew Bergschneider,[2] Jacob Spiegelman,[1] Harsono Simka,[3] Kyeongjae Cho,[2] and Andrew C. Kummel[4]

AFFILIATIONS

[1] Material Science and Engineering Program, University of California San Diego, La Jolla, California 92093
[2] Department of Materials Science and Engineering, University of Texas at Dallas, Dallas, Texas 75083
[3] Logic Pathfinding Lab, Samsung Semiconductor Inc., San Jose, California 95134
[4] Department of Chemistry and Biochemistry, University of California San Diego, La Jolla, California 92093

[a] **Author to whom correspondence should be addressed:** viw031@eng.ucsd.edu

ABSTRACT

Ruthenium (Ru) is an alternative to copper (Cu) and cobalt (Co) interconnect layers in sub 20 nm features due to its low resistivity in scaled wires and low diffusion into porous low-K dielectrics (SiCOH). Two goals for a successful Ru atomic layer deposition (ALD) process are to enable films with resistivity values as close as possible to that of bulk Ru and to enable selective deposition to achieve bottom-up fill of vias. In this work, the effects of dose variation on resistivity and selectivity of the Ru ALD process using a dicarbonyl-bis(5-methyl-2, 4-hexanediketonato) Ru(II) precursor, Ru(IHD)$_2$(CO)$_2$ ("Carish"), and O_2/He coreactant were investigated. Instead of varying the Carish precursor dose to optimize the growth rate per cycle, the precursor dose was optimized to reduce the film resistivity from 18.5 to 10.2 $\mu\Omega$ cm. By varying the O_2/He coreactant dose, the substrate selectivity of the ALD process was successfully enhanced as evidenced by the increased nucleation delay on bis(N,N-dimethylamino)dimethylsilane passivated SiO_2 over hydrofluoric acid-cleaned SiO_2. These findings highlight the importance of dose optimization beyond the ALD saturation point in developing a selective and low resistivity Ru ALD process. Density functional theory calculations were performed to provide a mechanistic understanding of the underlying surface reactions of the Carish precursor and the roles of CH_3 passivation and O_2 coreactants.

I. INTRODUCTION

With increased scaling of interconnects, the resistance of copper (Cu) interconnect lines rapidly increases when the critical dimensions become shorter than the Cu mean free path and/or when the diffusion barriers to porous low-k dielectrics occupy a significant fraction of the cross-sectional area.[1–7] Ruthenium (Ru) with its low bulk resistivity ($\sim$7 $\mu\Omega$ cm) is a compelling candidate to replace Cu due to its smaller inelastic mean free path resulting in a weaker dependence on interconnect dimensions.[8] In addition, Ru does not require a diffusion barrier to SiCOH, thereby allowing the use of a full cross section of the vias and lines for conduction in Ru.

The growth of Ru films via atomic layer deposition (ALD) is attractive because of ALD's ability to deposit highly conformal films with Angstrom-level thickness control on high aspect ratio features.[9] Furthermore, area selective ALD can enable vertical via-fill without unwanted air gaps by preventing material growth along the sidewalls. Area selective ALD of Ru had been achieved using bis(N, N-dimethylamino)dimethylsilane (DMADMS) to deposit CH_3 inhibitors that adsorb only onto SiO_2 surfaces and not Si surfaces.[10] In addition to demonstrating area selective deposition, achieving low resistivity Ru ALD films is critical to its adoption as a new interconnect conductor. Current ALD processes for Ru metal exhibit resistivity values ranging from 10 to 40 $\mu\Omega$ cm[9–38] while PVD-grown Ru films have exhibited resistivities as low as 8.2 $\mu\Omega$ cm.[39] A range of precursors have been investigated for ALD processes including Ru(EtCp)$_2$, Ru(thd)$_3$, Ru(DMBD)(CO)$_3$, and EBBD(Ru). However, the Ru ALD processes that yield the lowest resistivity films all use oxygen as the coreactant in a combustion ALD process. While most of these processes demonstrate precursor pulse saturation, the effect of precursor pulse variation on film resistivity and selectivity has not yet been investigated.

In the present work, Ru ALD was performed using a dicarbonyl-bis(5-methyl-2, 4-hexanediketonato) Ru(II) precursor or Ru(IHD)$_2$(CO)$_2$ ("Ru-Carish," Tanaka Kikinzoku Int'l.) with O_2 at a 300 °C deposition temperature. While studies using the same precursor and coreactant have been published using growth-based optimization, the lowest resistivity found in the literature with this process is 16 $\mu\Omega$ cm[40] while other published results had resistivities as high as 20 $\mu\Omega$ cm[41] which are much higher than the resistivity reported in the present work (see Fig. 1). Growth-based optimization is the traditional method to ensure that the deposition will be conformal since the pulse lengths are chosen to be just above the threshold for saturated growth per cycle. However, the electrical properties of the films may be dependent on the removal of trace contaminants which cannot be determined from the growth rate per cycle. Therefore, multiple measurements were made to characterize the films. Deposited films for this work were characterized using *in situ* x-ray photoelectron spectroscopy (XPS) for chemical composition, and *ex situ* measurements including atomic force microscopy (AFM) for surface roughness, x-ray reflectometry (XRR) for thickness, and 4-point probe for sheet resistance. The effects of precursor pulse variation on surface roughness, film purity, and resistivity elucidated a proposed mechanism for consistently achieving Ru films with resistivity as low as 10.2 $\mu\Omega$ cm without forming a gas anneal. The importance of precursor pulse variation is further highlighted by its ability to extend the nucleation delay on a DMADMS passivated SiO_2, thus enhancing the ALD substrate selectivity.

II. EXPERIMENT

A. Methods

For the presented Ru ALD process, a 10% O_2/He mixture was used instead of pure O_2 due to the limitations of the ALD pulse valve actuation time. The ALD pulse valves have a minimum actuation time of 15 ms, which would result in too large of an O_2 dose when using pure O_2, so a diluted 10% O_2/He mixture was used instead.

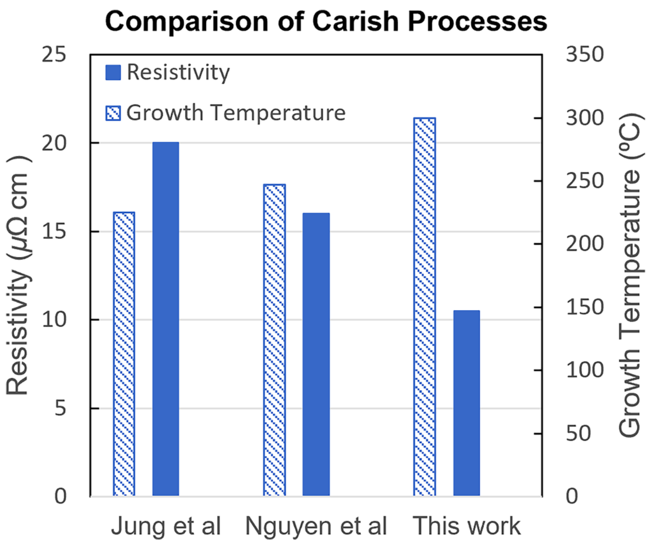

FIG. 1. Resistivity and growth temperature comparison between this work and other works in the literature using the Carish precursor. The two cited works in this comparison report the current best resistivity values in the literature for Ru ALD using the Carish precursor (Refs. 40 and 41).

The deposition chamber was pumped by a Pfeifer TPH062 turbomolecular pump, which limited the maximum chamber pressure without damaging the turbomolecular pump. A turbomolecular pump was employed to ensure a low concentration of background contaminants during ALD. Operating at a chamber pressure higher than roughly 1 Torr can damage the blades of the turbomolecular pump. Consequently, dose variation was achieved by using multiple pulses in each cycle to reach the same effective Langmuir dose as in ALD with an increased pulse length, while keeping the deposition chamber pressure low enough to ensure the safe operation of the turbomolecular pump. The number of pulses will be used to describe the number of precursor or coreactant pulses used in each dose variation condition per cycle. The timing of multiple pulses has been optimized such that the process pressure is stable from the peak pressure after the first pulse until the last pulse before purging. This ensures a stable and controlled variation on the Langmuir dosing based on the number of pulses. Others have shown that splitting precursor or passivation doses into discreet pulses via the discreet feeding method can help to improve film quality or selectivity.[42–47] However, the present work seeks to explore the effects of varying the total amount of precursor and coreactant dosed during ALD growth while keeping the precursor and coreactant feeding method consistent with the same interval between discreet pulses to achieve record low resistivity and enhanced selectivity for an ALD process with the Carish precursor.

Before deposition, samples were degreased and dipped in 0.5% HF (hydrofluoric acid) solution for 30 s, followed by a 30 min ultrahigh vacuum anneal at 350 °C to remove atmospheric contaminants. After deposition, samples were transferred without breaking the vacuum to a UHV chamber for XPS (Scienta Omicron). Due to the identical binding energy of C1s and Ru3d orbitals, definitive deconvolution of the two was not possible, and only a rough estimate of carbon was given in the XPS analysis. The primary goals of the XPS analysis were to determine the selectivity of the deposition, the oxygen content in the film, and the chemical state of the ruthenium.

Ex situ four-point probe (Ossila Four-Point Probe System, Ossila, Ltd.) measurements were performed to measure the sheet resistance. The film dimensions were $6 \times 2\ \text{mm}^2$ with a probe spacing of 1.27 mm, which required a geometric factor of 0.3443 to be applied to the sheet resistance to correct for errors introduced by the semi-infinite film approximation. XRR (Rigaku Smartlab) was performed for thickness measurements, which were used in conjunction with the sheet resistance to derive a resistivity value. For the XRR measurements, a tube voltage of 40 kV and a tube current of 44 mA were used.

B. Results and discussion

Using a 300 °C stage temperature, Ru films were deposited over a range of thicknesses, 30, 45, and 135 nm, using pulsing parameters optimized for low resistivity films: four pulses of 400 ms Ru(IHD)$_2$(CO)$_2$ and two pulses of 20 ms O_2/He using a purge time of 60 s and a 1 s pump out between each pulse. Figure 2 shows the thickness, density, sheet resistance, and resistivity of Ru ALD samples deposited using 75, 150, and 500 cycles. XRR oscillations and fit used to calculate the densities and thicknesses are shown in Fig. S1 in the supplementary material.[67] The close fit of the modeled curve and the measured oscillations established confidence in the thickness values used to derive the resistivity values. Additionally, XRD spectra are shown in Fig. S2 in the supplementary material,[67] exhibiting crystallinity in the three films. The relative intensity of the XRD peaks is related to the ratio of textures in the Ru film grown relative to plane directions. At this point, there is no process variation known to control this ratio of textures in deposited films; furthermore, despite similar dosing conditions, the textures can still vary consistent with a dependence on substrate defect density.

Measurements were performed on different areas of each sample to check for variations in measured values that may be caused by surface roughness. Measurements across multiple areas showed negligible differences in thickness establishing confidence in the values.

The ALD process had film thicknesses of 30, 44, and 130 nm for 75, 150, and 500 cycles of deposition, respectively. Densification of the film with additional cycles may be the cause of the differences in growth rate. Although the XRR fit for density may not be ideal due to film roughness, density values are shown for a relative comparison between the films and should not be taken as absolute density values. It is noted that with increasing density, the resistivity of the films decreases. This is consistent with better crystallinity and/or lower contamination content leading to lower resistivity

Nguyen *et al.* have shown that in depositing Ru metal via ALD, over-exposure to O_2 can lead to RuO_x formation.[40] In this work, *in situ* XPS has been done on all of the deposited films to ensure that they are metallic and there is negligible residual oxygen on the surface of Ru. Consequently, any increase in resistivity from changes in the precursor or coreactant dose may stem from oxygen contamination within grain boundaries but is unlikely to be due to ruthenium oxide surface deposition. Figure 3 shows the XPS Ru 3d spectra, confirming the deposited films to be metallic ruthenium instead of RuO_x, and the films having very low oxygen contamination levels. The Ru 3d peaks match well with literature values for metallic ruthenium peak at 280.12 eV binding energy rather than 281.05 eV for RuO_x.[42] In addition, the oxygen spectra shown in Fig. S3 in the supplementary material[67] for these samples exhibited negligible peaks, consistent with metallic ruthenium deposition. The oxygen content of the films can also be indicative of contamination in the grain boundaries. The low oxygen contents are consistent with the low resistivity values. For all three metallic ruthenium samples, oxygen content and resistivities were consistently low, demonstrating that the ALD process was robust and repeatable.

While pulse saturation for ALD processes is important to realize self-limiting growth, the optimization of precursor dose for resistivity rather than growth saturation can yield lower resistivity films. The optimal precursor dose for Ru resistivity was quantified by the number of 250 ms precursor pulses for each ALD cycle. A Carish dose variation study is shown in Fig. 4. The sample using four pulses of Carish, as opposed to two pulses of Carish, exhibited a higher RMS surface roughness and a lower oxygen content. The related XRR is shown in Fig. S4 in the supplementary material,[67] and the resulting resistivities are shown in Fig. 4. The significant reduction in film resistivity from 18.5 to 10.2 $\mu\Omega$ cm with a 2× increase in the Carish dose is consistent with increased grain sizes derived from XRD using the Scherrer equation as shown in Fig. S5 in the supplementary material.[67] The larger grains can be a result of a more complete reaction per cycle due to the increased precursor dose or additional purge time allowing more time for surface species to react. Several authors have documented longer cycle

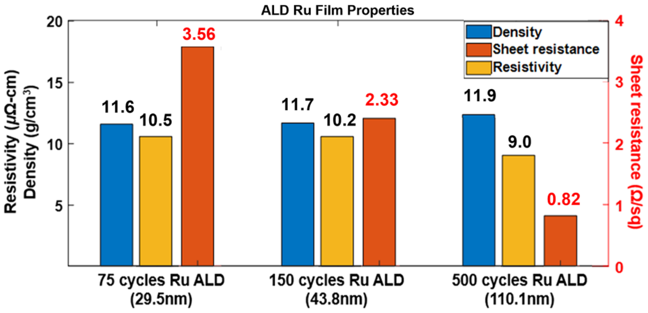

FIG. 2. Thickness, density, resistivity, and sheet resistance for the three samples with 75, 150, and 500 cycles of Ru ALD. The thicknesses and densities were measured via XRR. XRR oscillations and fit are shown in Fig. S1 in the supplementary material. Sheet resistance was measured via four-point probe. Resistivities were derived from thickness and sheet resistance.

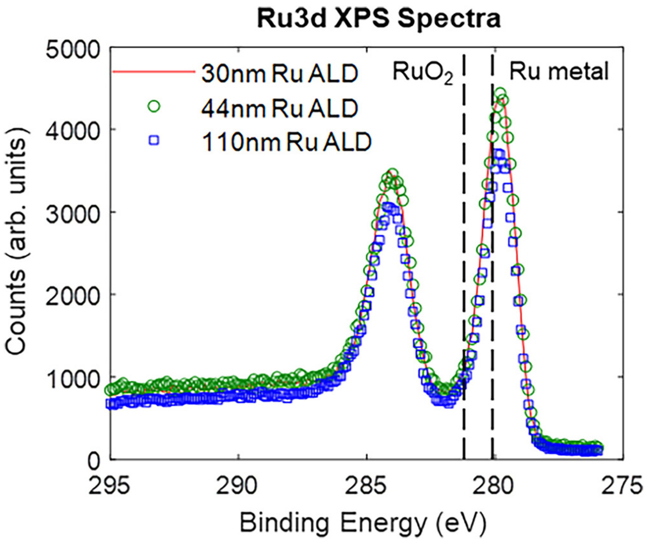

FIG. 3. XPS Ru 3d spectra for samples with 30, 44, and 110 nm of Ru ALD growth: Ru 3d XPS spectra for samples with varying thicknesses. Binding energies shown by peaks indicate metallic growth and not oxide growth when compared to literature values.

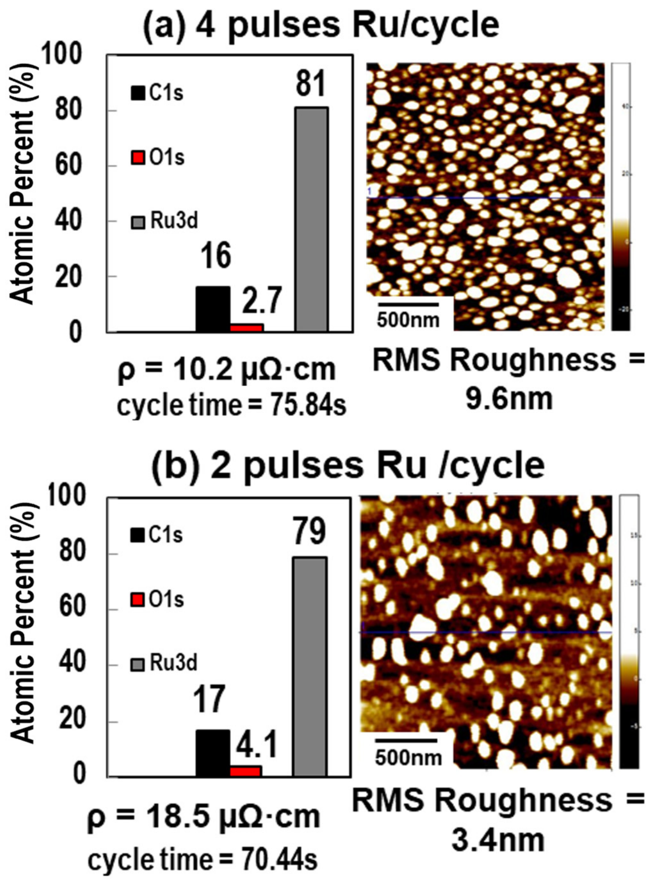

FIG. 4. XPS analysis and AFM of deposited films with varying $\mathrm{Ru(IHD)_2(CO)_2}$ doses for 150 cycles of ALD at 300C: (a) four pulses of $\mathrm{Ru(IHD)_2(CO)_2}$ per cycle and (b) two pulses of $\mathrm{Ru(IHD)_2(CO)_2}$ per cycle. As the $\mathrm{Ru(IHD)_2(CO)_2}$ dose is increased, the RMS roughness increases, and the oxygen content decreases. The XRR and four-point probe measurements (Fig. S3 in the supplementary material) show that the higher $\mathrm{Ru(IHD)_2(CO)_2}$ dose reduced the resistivity.

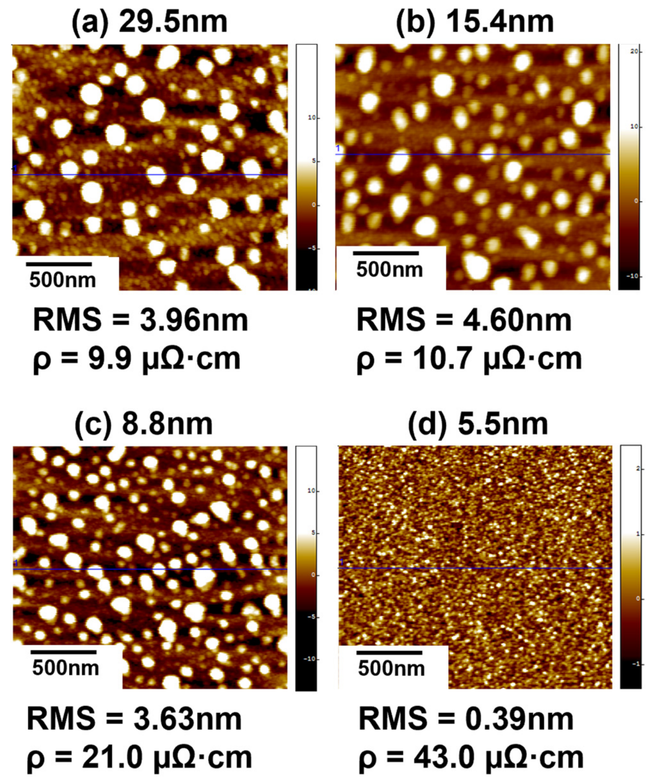

FIG. 5. AFM images and RMS surface roughness values for samples with varying thicknesses of deposited Ru on HF-cleaned Si. The deposited films were (a) 29.5, (b) 15.4, (c) 8.8, and (d) 5.5 nm. RMS surface roughness does not increase film resistivity at higher thicknesses.

times that can improve the electrical resistance of deposited metal films.[42,45,46,49,50] However, when comparing the cycle times for the 2× and 4× Carish doses, the total cycle time is dominated by the long purge times between the Carish and O_2 pulses. Therefore, the difference in total cycle times is just 75.84 versus 70.44 s so the data are most consistent with the primary effect of the 2× greater Carish dose than the 7.1% increase in cycle times. Density values were not obtained due to poor fitting from XRR, likely due to surface roughness effects.

While this reduction in resistivity can be attributed also to the difference in thickness, the 4× Carish pulse condition also yielded a 15.4 nm film with comparably low resistivity of $10.7\,\mu\Omega\,\mathrm{cm}$. The 43.8 nm film was used as the benchmark for comparison because it was the lower resistivity sample. The reduction in resistivity could be also attributed to the lower oxygen content. Less oxygen contamination in the grain boundaries can decrease the reflectance coefficient for electrons at each boundary and decrease the overall film resistivity.[51] Similarly, higher surface roughness could also be indicative of larger grains in the film.[38]

A comparison of AFM images of samples with different thicknesses deposited with the fixed dosing condition of 4× Carish pulses and 2× O_2/He pulses shows that variation in RMS surface roughness does not lead to high resistivity in thick films. Figure 5 shows a series of AFM images for varying thickness films along with their RMS surface roughness and resistivity values. The XRR oscillations and fits are shown in Fig. S6 in the supplementary material.[67] Despite the lower RMS surface roughness values of 3.96 and 4.60 nm, the resistivity for the 15.4 and 29.5 nm films are still relatively low at 10.7 and $9.9\,\mu\Omega\,\mathrm{cm}$, respectively, comparable to the film shown in Fig. 4 with a higher 9.6 nm RMS roughness and $10.2\,\mu\Omega\,\mathrm{cm}$ resistivity. Despite the vastly different RMS roughness, there is not a significant difference in resistivity, which suggests that a correlation between RMS roughness and resistivity cannot be observed. When the film thickness decreases below a critical value, the resistivity increases for films with both high RMS roughness (3.63 nm) and low RMS roughness (0.39 nm), as shown in Fig. 5. The data are consistent with resistivity changes being independent of roughness once a continuous film of several nanometers has formed.

Using a recently proposed model for metal resistivity (Gall *et al.*), the overall film resistivity can be split into three components: bulk resistivity, a surface scattering component, and a grain boundary scattering component.[51] The surface scattering component is dependent on the film thickness and a specularity constant related to the metal–vacuum interface; note the resistance measurements were made in the atmosphere, but Ru only has a monolayer of oxidation so the model should be reasonable for the present study. The grain boundary component is dependent on the grain size and the electron reflectivity coefficient. When the metal film becomes sufficiently thin, the surface scattering component begins to dominate, resulting in a high resistivity regardless of the grain boundary scattering component contribution.[51] The data are consistent with the model of Gall *et al.* when film thicknesses are less than 15.4 nm. However, thicker samples shown in Figs. 4(a), 5(a), and 5(b) exhibit low resistivity despite varying degrees of high RMS surface roughness value. If the surface roughness does not play a role in determining the film resistivity, the resistivity may be dominated by the oxygen content of the film or grain boundaries or just simply the grain size. Lower oxygen content in the film can be indicative of less contamination in the grain boundaries, which would result in a lower electron reflectivity coefficient and, subsequently, lower film resistivity. Meanwhile, larger grains in the films mean fewer grain boundaries for the electrons to traverse.

From an analysis of the AFM images, the aspect ratios of particles were determined. The particle heights are much smaller than particle lateral areas resulting in flat "disk-like particles." The particles are denoted as "disk-like" since unlike typical metallic grains with diameter/height aspect ratios <1, the surface feature of diameter/height ratio ≫ 1. Figure 6 shows a plot of surface particle peak height to particle area. The constant slope in Fig. 6 is consistent with the approximately constant aspect ratio (diameter/height) of the nuclei. The average aspect ratios are 10.0, 10.1, and 8.4, while the average diameters are 141, 133, and 112 for the 30, 15, and 9 nm thick films. While the lateral resolution of the AFM is limited due to the shape of the tip, grain area uncertainty around 314 nm^2 is expected with the 10 nm radius tip. This uncertainty, however, is negligible for the results shown since grain areas greater than 5000 nm^2 are being compared. The reported mean free path of an electron in the Ru is 6.7 nm for (0001) Ru;[48] since the nuclei diameters are more than 10× greater than the mean free path, it is reasonable that the disk particles do not increase the resistivity of the film despite increasing the RMS roughness. These data suggest that RMS roughness does not necessarily indicate large grain sizes in the film and low resistivity.

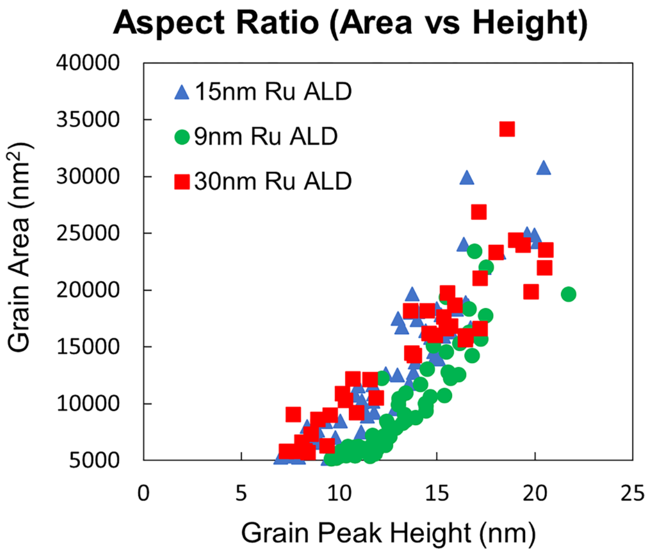

FIG. 6. Plot of grain peak height to grain area. The aspect ratio is nearly constant in each sample as shown by an almost constant slope in the plot.

The oxygen reducing effects of varying the Carish precursor dose could stem from balancing the ALD precursor and coreactant when nucleating on the sample surface. Aaltonen *et al.* have shown that oxygen adsorption on the initial sample surface is required for the Carish to react and form Ru metal via a combustion reaction.[11] However, an insufficient Carish dose may leave behind excess oxygen on the sample surface that may become contaminants in the deposited film. Furthermore, an insufficient Carish dose can also result in incomplete oxygen removal per cycle resulting in lower quality films with smaller grain sizes. Consequently, a sufficient Carish dose is necessary to both form a monolayer on the sample surface and minimize residual oxygen in the film. In the present study, variation in the Carish dose helped to establish a better balance in the precursor to coreactant dose ratio, which resulted in a higher quality film with lower resistivity.

In addition to low resistivity, substrate selectivity was also achieved with the Carish process when comparing growth on an HF-cleaned SiO_2 substrate and a DMADMS passivated SiO_2 substrate. Although inherent selectivity was not present in this process, nucleation differences were achieved after DMADMS passivation. Growth is observed on the HF-cleaned SiO_2 earlier than on the DMADMS passivated SiO_2 due to a nucleation delay induced by the CH_3 termination on the DMADMS passivated SiO_2 surface consistent with the study by Khan *et al.*[10] Figure 7 shows an O_2/He dose variation study via the XPS analysis of sample surfaces as loaded, after 50 cycles of Ru ALD, and after 50 more cycles of Ru ALD on both HF-cleaned SiO_2 and DMADMS passivated SiO_2. Despite having little effect on the growth of HF-cleaned SiO_2, the O_2/He dose variation enhanced selectivity by extending the nucleation delay on the DMADMS passivated SiO_2.

III. MODELING

To develop a mechanistic understanding of the Carish precursor reactions on several substrates, density functional theory (DFT) calculations were performed for Carish precursor in the gas phase, OH-terminated SiO_2 surface with and without oxygen coreactants, and CH_3-terminated SiO_2 surface. DFT calculations were performed using the Vienna *Ab Initio* Simulation Package,[52] using the projector-augmented wave method in a plane-wave basis set.[53,54] The generalized gradient approximation (GGA) method was

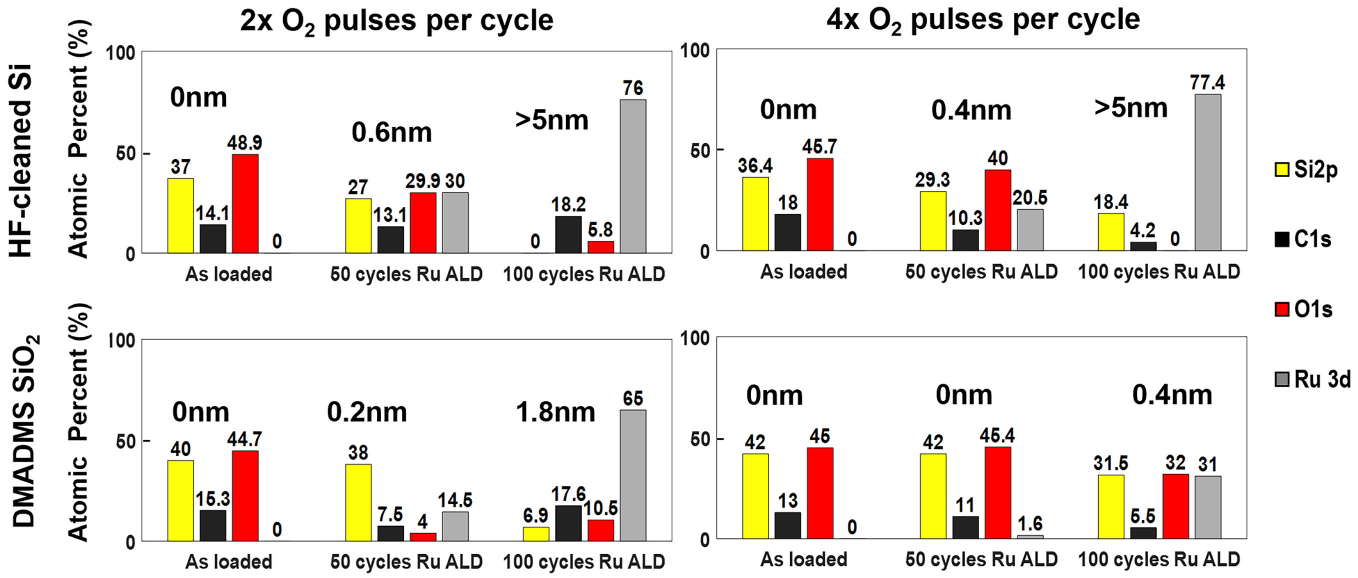

FIG. 7. XPS analysis showing O_2/He dose variation effects on both HF-cleaned SiO_2 and DMADMS passivated SiO_2. Thickness estimates based on substrate signal attenuation are given.

employed using Perdew–Berke–Ernzerhof[55] functional for all calculations. Accurate energy calculations for elements with strongly correlated orbitals were achieved through the application of the GGA + U method.[56,57] Gamma-centered reciprocal-space grids with a minimum spacing of 0.003 nm^{-1} and 500 eV kinetic energy cutoff were used. Atoms in supercells were allowed to relax with fixed volume, for –OH and $-CH_3$-terminated SiO_2 slabs of 7.4 Å thickness, including a vacuum layer of at least a 15 Å thickness. Each supercell was relaxed to force-based convergence criteria of 0.001 $eV{\cdot}nm^{-1}$. Calculations were spin-polarized where the magnetic moments for the Ru structures were accounted for with the GGA + U corrections of Dudarev *et al.*[58] with a relatively small U_{eff} value of 1.2 eV being used for the Ru oxide. This U_{eff} value was determined by matching the calculated formation enthalpy of crystalline RuO_2 to that reported by O'Neill and Nell[59] DFT-D2 van der Waals correction method of Grimme[60] was replaced with DFT-dDsC dispersion correction to better account for local surface chemistry environment.[61–63]

The reaction states for Carish precursor ligand dissociation have been modeled for CH_3-terminated SiO_2, OH-terminated SiO_2, and OH-terminated SiO_2 in an oxygen-rich environment. The surfaces are modeled by a slab geometry with 3D periodic boundary conditions and 9–15 Å of vacuum to reduce image interaction and accommodate the bulky molecule. Because the density of β-cristobalite (2.20 $g\,cm^{-3}$) and amorphous SiO_2 (2.19 $g\,cm^{-3}$) are very similar, a 2 × 2 cristobalite bulk structure was cut along the (100) plane and saturated with hydrogen/hydroxyls to mimic amorphous SiO_2 surface. The dangling bonds of silicon were saturated with hydroxyl groups to satisfy tetragonal coordination, and the dangling bonds of oxygen were saturated with hydrogen to satisfy twofold coordination as in bulk SiO_2, which we found to be most energetically favorable and agreeable with the previous modeling works. The methyl-terminated surface was chosen as a representative case of DMADMS reaction with the oxide surface, which would yield a mixture of $-NH_3$, $^*O_2-Si(CH_3)_2$, or $^*O_3-SiCH_3$.[64] In the interest of clarity, we selected the latter and constructed the surface by substitution of one hydroxyl for a methyl group on each of the eight silicon atoms on one surface, yielding the $^*O_3-SiCH_3$ terminal surface, which shows sufficient passivating behavior. The opposing, noninteracting surface of the slab retained OH termination, with the freedom to relax, reducing artifacts of polarity at the surfaces. Figure 8 illustrates the individual steps assumed for the precursor dissociation on the three surfaces. State number 1 reflects the precursor $Ru(IHD)_2(CO)_2$ adsorption on the surface. Here, "*" denotes surface site adsorption. Step 2 depicts the dissociation of $Ru(IHD)_2(CO)_2$ to $Ru(IHD)_2(CO)$ and (CO) on the surface. Step 3 shows further dissociation to $Ru(IHD)_2$ and (CO) on the surface. Steps 4 and 5 follow further dissociation of $Ru(IHD)_2$ to Ru(IHD) and (IHD), then dissociation of Ru(IHD) to Ru and (IHD), where the presence of oxygen becomes significant. The dissociation steps on OH-terminated SiO_2 (shown in column 2 of Fig. 8) can be summarized with the following reaction states:

State 0: $Ru(IHD)_2(CO)_2(g) \rightarrow$
State 1: $^*Ru(IHD)_2(CO)_2 \rightarrow$
State 2: $^*Ru(IHD)_2(CO) + {}^*CO \rightarrow$
State 3: $^*Ru(IHD)_2 + 2{}^*CO \rightarrow$
State 4: $^*Ru(IHD)_2 + 2{}^*CO + {}^*IHD \rightarrow$
State 5: $^*Ru + 2{}^*CO + 2{}^*IHD \rightarrow$

Such adsorption energy steps have been considered in recent works for implementation in Monte Carlo methods of calculating growth per cycle.[65,66] These works relied on the gas layer approximation in 2D and 3D considering steric hindrances to the

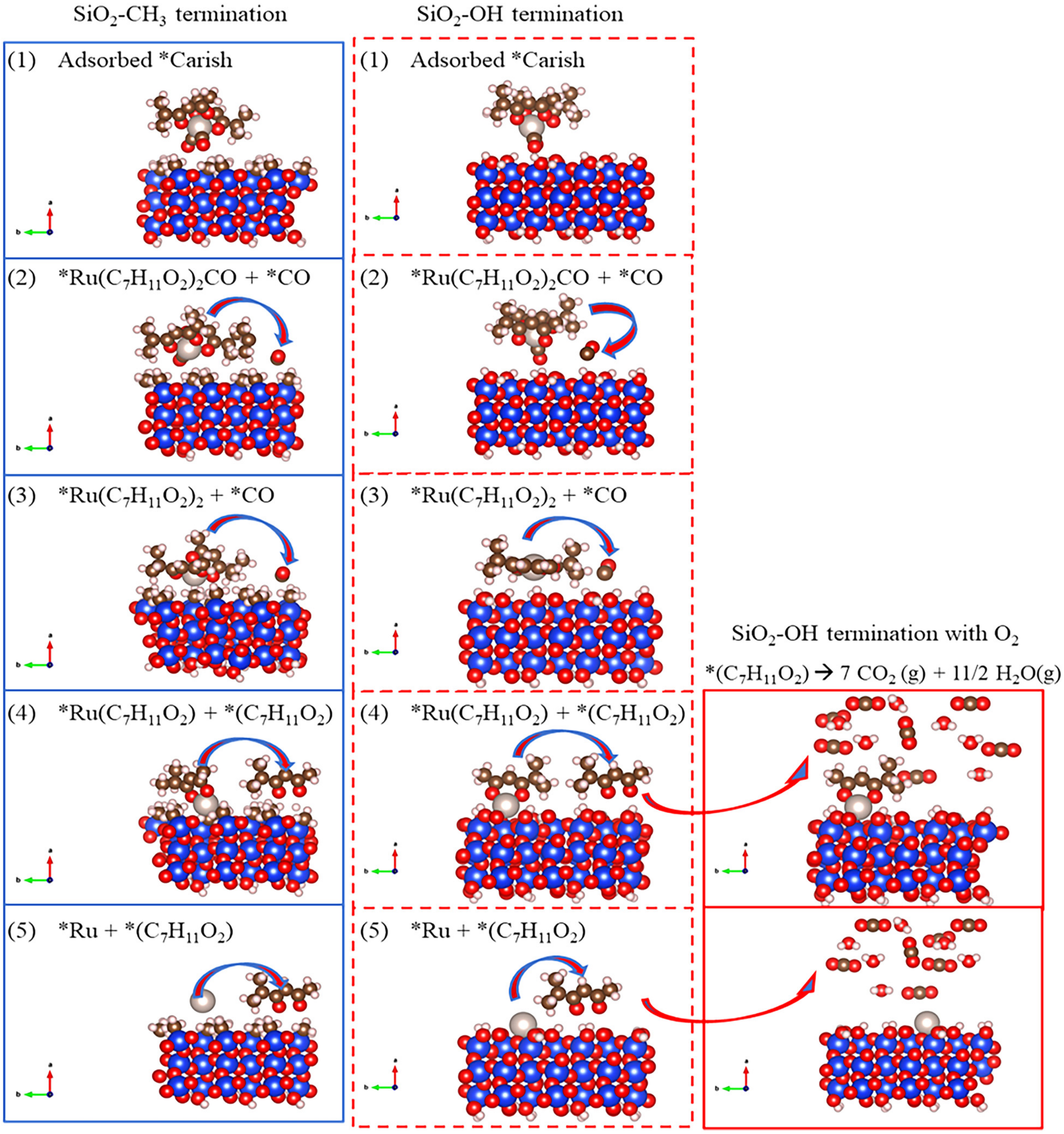

FIG. 8. Dissociation states in step numbers of Ru Carish on SiO_2 with CH_3 termination, OH termination, and OH termination in O_2-rich environment. The resulting Ru atom is weakly physiosorbed onto the sample substrate in the case of CH_3 termination as compared to a more strongly adsorbed result in the case of OH termination.

adsorption of bulky precursor molecules and consideration of the metal, H-terminal, or $Al(CH_3)_2/AlCH_3$ (DMA/MMA) passivated surface sites, and are in agreement with the work presented here, but do not consider the following side reactions. In an O_2-rich environment, combustion of IHD ligands would also occur; this is shown in column 3 of Fig. 8. The dissociation steps on OH-terminated SiO_2 in an O_2-rich environment can be summarized with the following reaction states:

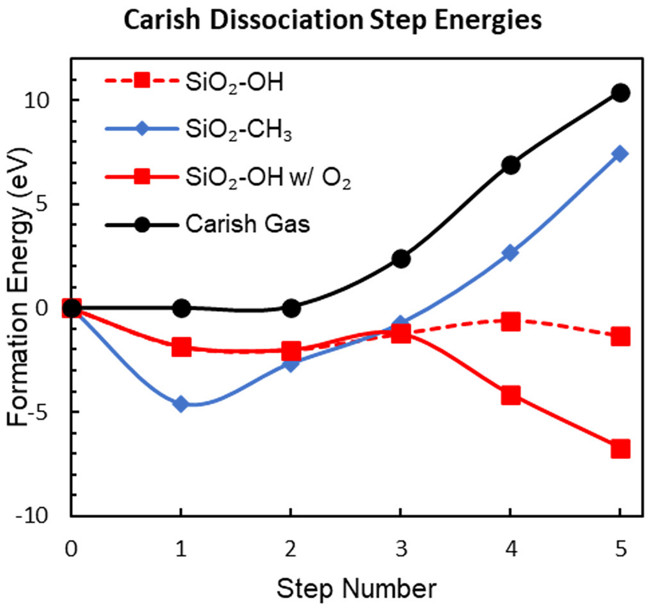

FIG. 9. Formation energy vs nucleation step number for $Ru(IHD)_2(CO)_2$ on different surfaces. SiO_2 with OH termination is much more favorable for Ru $(IHD)_2(CO)_2$ nucleation than SiO_2 with CH_3 termination, which is consistent with the experimental results of comparing nucleation between HF-cleaned SiO_2 and DMADMS passivated SiO_2.

State 0: $Ru(IHD)_2(CO)_2(g)\ + * \rightarrow$
State 1: $*Ru(IHD)_2(CO)_2 + * \rightarrow$
State 2: $*Ru(IHD)_2(CO) + *CO + * \rightarrow$
State 3: $*Ru(IHD)_2 + 2\ (*CO) + 35/2\ O_2(g) \rightarrow$
State 4: $*Ru(IHD) + 2\ (*CO) + 7\ CO_2\ (g)\ + 11/2\ H_2O\ (g)$
$+ 35/2\ O_2(g) \rightarrow$
State 5: $*Ru + 2\ (*CO) + 14\ CO_2\ (g)\ + 11\ H_2O\ (g)$

The calculated formation energies shown in Fig. 9 follow the dissociation of Ru-Carish precursor ligands on the respective surfaces with and without physisorbed O_2 from the environment. The step numbers on the x-axis follow the previously outlined dissociation states.

Surface oxygen of the −OH terminal SiO_2 reacts with the (IHD) ligand, driving the reaction to be exothermic for the combustive dissociation of IHD, and excess O_2 refills the resultant empty surface site to be −OH terminated. As such, the model of nucleation of Ru and subsequent growth is thermodynamically favorable and matches with experimental data shown in Fig. 7 where growth is favored on HF-cleaned Si. In the case of methyl-terminated SiO_2, methyl termination prevents the ligands from strongly bonding to the surface, and the CH_3-passivated surface suppresses Carish reactions on the surface preventing Ru metal atoms to nucleate and bond to the surface which is the first step in Ru film growth. In an oxygen-rich environment, the presence of physisorbed O_2 on SiO_2 may decompose the precursor ligands for small O_2 doses, but additionally oxidize Ru to RuO_2 and RuO_4 for larger O_2 doses with binding energies of −2.23, −0.628, and 0.02 eV, respectively. With negligible binding to the surface, the RuO_4 will desorb from the surface, thus sufficient O_2 may act as an etchant of any initially nucleated Ru. This effect is consistent with experimental observation showing that additional oxygen dose enhances passivation against Ru growth.

IV. SUMMARY AND CONCLUSIONS

Low resistivity ruthenium films were deposited via ALD at 300 °C with $Ru(IHD)_2(CO)_2$ and 10% O_2/He mixture as precursor and coreactant. XPS analysis indicated that an increase of 2× in $Ru(IHD)_2(CO)_2$ dose beyond that required for growth rate saturation reduced the oxygen content in the deposited film by nearly a factor of two and reduced resistivity by a factor of two. Although RMS surface roughness obtained via AFM increased with the excess $Ru(IHD)_2(CO)_2$ dose, the effect of RMS surface roughness on resistivity was found to be negligible for films above 13 nm thickness. This may be due to particles on the surface being too small to affect resistivity, but large enough to exhibit a high RMS roughness. Precursor dose optimization beyond pulse saturation for self-limiting growth may be vital to producing low resistivity metal films due to their role in balancing precursor and coreactant for complete nucleation without leaving excess oxygen on the surface that may become contaminants in grain boundaries, thus making low resistivities around $10\,\mu\Omega$ cm possible without postdeposition annealing. Excess oxygen dosing beyond that required for growth saturation increases deposition selectivity on unpassivated SiO_2 compared to passivated SiO_2. This is consistent with excess oxygen removing Ru nucleation on defects on the passivated SiO_2.

ACKNOWLEDGMENTS

This work was supported by the Semiconductor Research Corporation.

AUTHOR DECLARATIONS

Conflict of Interest

The authors have no conflicts to disclose.

Author Contributions

Victor Wang: Data curation (equal); Formal analysis (equal); Investigation (equal); Methodology (equal); Project administration (equal); Software (equal); Visualization (equal); Writing – original draft (lead); Writing – review & editing (lead). **Michael Breeden:** Data curation (equal); Formal analysis (equal); Investigation (equal); Methodology (equal); Project administration (equal); Software (equal); Visualization (equal). **Nickolas Ashburn:** Data curation (supporting); Formal analysis (supporting); Software (equal); Visualization (equal); Writing – original draft (supporting). **Matthew Bergschneider:** Data curation (supporting); Formal analysis (supporting); Software (equal); Visualization (equal); Writing – original draft (supporting). **Jacob Spiegelman:** Formal analysis (supporting); Software (supporting). **Harsono Simka:** Formal analysis (equal); Writing – review & editing (supporting). **Kyeongjae Cho:** Supervision (equal); Writing – review & editing (supporting). **Andrew C. Kummel:** Conceptualization (lead); Project administration (lead); Supervision (lead); Writing – review & editing (equal).

DATA AVAILABILITY

The data that support the findings of this study are available from the corresponding author upon reasonable request.

REFERENCES

[1] B. Wu and A. Kumar, Appl. Phys. Rev. **1**, 011104 (2014).
[2] K. Barmak, X. Liu, A. Darbal, N. T. Nuhfer, D. Choi, T. Sun, A. P. Warren, K. R. Coffey, and M. F. Toney, J. Appl. Phys. **120**, 065106 (2016).
[3] J. S. Chawla, F. Gstrein, K. P. O'Brien, J. S. Clarke, and D. Gall, Phys. Rev. B **84**, 235423 (2011).
[4] T. Sun, B. Yao, A. P. Warren, K. Barmak, M. F. Toney, R. E. Peale, and K. R. Coffey, Phys. Rev. B **81**, 155454 (2010).
[5] D. Josell, S. H. Brongersma, and Z. Tokei, Annu. Rev. Mater. Res. **39**, 231 (2009).
[6] J. J. Plombon, E. Andideh, V. M. Dubin, and J. Maiz, Appl. Phys. Lett. **89**, 113124 (2006).
[7] K. Barmak *et al.*, J. Vac. Sci. Technol. A **38**, 033406 (2020).
[8] C. Adelmann *et al.*, in *2014 IEEE International Interconnect Technology Conference/Advanced Metallization Conference, IITC/AMC 2014* (IEEE, New York, 2014).
[9] S. Cwik, K. N. Woods, M. J. Saly, T. J. Knisley, and C. H. Winter, J. Vac. Sci. Technol. A **38**, 012402 (2020).
[10] R. Khan *et al.*, Chem. Mater. **30**, 7603 (2018).
[11] T. Aaltonen, P. Alén, M. Ritala, and M. Leskelä, Chem. Vapor Depos. **9**, 45 (2003).
[12] O.-K. Kwon, J.-H. Kim, H.-S. Park, and S.-W. Kang, J. Electrochem. Soc. **151**, G109 (2004).
[13] T. Aaltonen, M. Ritala, K. Arstila, J. Keinonen, and M. Leskelä, Chem. Vapor Depos. **10**, 215 (2004).
[14] O. van der Straten, S. M. Rossnagel, J. P. Doyle, and K. P. Rodbell, ECS Trans. **1**, 51 (2019).
[15] K. J. Park, D. B. Terry, S. M. Stewart, and G. N. Parsons, Langmuir **23**, 6106 (2007).
[16] S.-H. Kwon, O.-K. Kwon, J.-H. Kim, S.-J. Jeong, S.-W. Kim, and S.-W. Kang, J. Electrochem. Soc. **154**, H773 (2007).
[17] S.-S. Yim, D.-J. Lee, K.-S. Kim, S.-H. Kim, T.-S. Yoon, and K.-B. Kim, J. Appl. Phys. **103**, 113509 (2008).
[18] S.-J. Park, W.-H. Kim, W. J. Maeng, Y. S. Yang, C. G. Park, H. Kim, K.-N. Lee, S.-W. Jung, and W. K. Seong, Thin Solid Films **516**, 7345 (2008).
[19] S.-J. Park, W.-H. Kim, H.-B.-R. Lee, W. J. Maeng, and H. Kim, Microelectron. Eng. **85**, 39 (2008).
[20] D.-J. Lee, S.-S. Yim, K.-S. Kim, S.-H. Kim, and K.-B. Kim, Electrochem. Solid State Lett. **11**, K61 (2008).
[21] W.-H. Kim, S.-J. Park, D. Kim, and H. Kim, J. Korean Phys. Soc. **55**, 32 (2009).
[22] T.-K. Eom, W. Sari, K.-J. Choi, W.-C. Shin, J. H. Kim, D.-J. Lee, K.-B. Kim, H. Sohn, and S.-H. Kim, Electrochem. Solid State Lett. **12**, D85 (2009).
[23] S. K. Park, R. Kanjolia, J. Anthis, R. Odedra, N. Boag, L. Wielunski, and Y. J. Chabal, Chem. Mater. **22**, 4867 (2010).
[24] D.-J. Lee, S.-S. Yim, K.-S. Kim, S.-H. Kim, and K.-B. Kim, J. Appl. Phys. **107**, 013707 (2010).
[25] S. K. Kim, J. H. Han, G. H. Kim, and C. S. Hwang, Chem. Mater. **22**, 2850 (2010).
[26] N. Leick, R. O. F. Verkuijlen, L. Lamagna, E. Langereis, S. Rushworth, F. Roozeboom, M. C. M. van de Sanden, and W. M. M. Kessels, J. Vac. Sci. Technol. A **29**, 021016 (2011).
[27] K. Kukli *et al.*, J. Electrochem. Soc. **158**, D158 (2011).
[28] K. Gregorczyk, L. Henn-Lecordier, J. Gatineau, C. Dussarrat, and G. Rubloff, Chem. Mater. **23**, 2650 (2011).
[29] S.-H. Choi, T. Cheon, S.-H. Kim, D.-H. Kang, G.-S. Park, and S. Kim, J. Electrochem. Soc. **158**, D351 (2011).
[30] R. Methaapanon, S. M. Geyer, H.-B.-R. Lee, and S. F. Bent, J. Mater. Chem. **22**, 25154 (2012).
[31] N. Leick, S. Agarwal, A. J. M. Mackus, and W. M. M. Kessels, Chem. Mater. **24**, 3696 (2012).
[32] K. Kukli *et al.*, Thin Solid Films **520**, 2756 (2012).
[33] M. Knaut, M. Junige, M. Albert, and J. W. Bartha, J. Vac. Sci. Technol. A **30**, 01A151 (2012).
[34] S.-H. Kim, ECS Trans. **41**, 19 (2019).
[35] S. Yeo, S. H. Choi, J. Y. Park, S. H. Kim, T. Cheon, B. Y. Lim, and S. Kim, Thin Solid Films **546**, 2 (2013).
[36] S. Yeo, J. Y. Park, S. J. Lee, D. J. Lee, J. H. Seo, and S. H. Kim, Microelectron. Eng. **137**, 16 (2015).
[37] M. Popovici *et al.*, Chem. Mater. **29**, 4654 (2017).
[38] D. Z. Austin, M. A. Jenkins, D. Allman, S. Hose, D. Price, C. L. Dezelah, and J. F. Conley, Chem. Mater. **29**, 1107 (2017).
[39] S. S. Ezzat, P. D. Mani, A. Khaniya, W. Kaden, D. Gall, K. Barmak, and K. R. Coffey, J. Vac. Sci. Technol. A **37**, 031516 (2019).
[40] C. T. Nguyen, J. Yoon, R. Khan, B. Shong, and H.-B.-R. Lee, Appl. Surf. Sci. **488**, 896 (2019).
[41] J.-H. Jung *et al.*, J. Nanosci. Nanotechnol. **15**, 8472 (2015).
[42] H. Wang, Z. Wang, X. Xu, Y. Liu, C. Chen, P. Chen, W. Hu, and Y. Duan, Appl. Phys. Lett. **114**, 201902 (2019).
[43] T. Muneshwar and K. Cadien, J. Appl. Phys. **119**, 085306 (2016).
[44] A. I. Aria, K. Nakanishi, L. Xiao, P. Braeuninger-Weimer, A. A. Sagade, J. A. Alexander-Webber, and S. Hofmann, ACS Appl. Mater. Interfaces **8**, 30564 (2016).
[45] J.-M. Lee, J. Lee, J. W. Han, H. Park, S. Kyung, I. W. Kim, J. M. Lee, T. J. Park, and W.-H. Kim, Appl. Surf. Sci. **539**, 148247 (2021).
[46] J. W. Han, H. S. Jin, Y. J. Kim, J. S. Heo, W.-H. Kim, J.-H. Ahn, J. H. Kim, and T. J. Park, Nano Lett. **22**, 4589 (2022).
[47] J. Lee, J.-M. Lee, J.-H. Ahn, T. J. Park, and W.-H. Kim, Adv. Mater. Interfaces **9**, 2102364 (2022).
[48] H. Over, A. P. Seitsonen, E. Lundgren, M. Smedh, and J. N. Andersen, Surf. Sci. **504**, L196 (2002).
[49] H. Song, D. Shin, J. Jeong, H. Park, and D.-H. Ko, AIP Adv. **9**, 035333 (2019).
[50] T. J. Park, J. H. Kim, J. H. Jang, U. K. Kim, S. Y. Lee, J. Lee, H. S. Jung, and C. S. Hwang, Chem. Mater. **23**, 1654 (2011).
[51] D. Gall, J. Appl. Phys. **127**, 050901 (2020).
[52] G. Kresse and J. Hafner, Phys. Rev. B **49**, 14251 (1994).
[53] G. Kresse and D. Joubert, Phys. Rev. B **59**, 1758 (1999).
[54] G. Kresse and J. Furthmüller, Phys. Rev. B **54**, 11169 (1996).
[55] J. P. Perdew, K. Burke, and M. Ernzerhof, Phys. Rev. Lett. **77**, 3865 (1996).
[56] G. Kresse and J. Furthmüller, Comput. Mater. Sci. **6**, 15 (1996).
[57] D. C. Langreth and M. J. Mehl, Phys. Rev. B **28**, 1809 (1983).
[58] S. L. Dudarev, G. A. Botton, S. Y. Savrasov, C. J. Humphreys, and A. P. Sutton, Phys. Rev. B **57**, 1505 (1998).
[59] H. St. C. O'Neill and J. Nell, Geochim. Cosmochim. Acta **61**, 5279 (1997).
[60] S. Grimme, J. Comput. Chem. **27**, 1787 (2006).
[61] S. N. Steinmann and C. Corminboeuf, J. Chem. Phys. **134**, 044117 (2011).
[62] R. Petraglia, S. N. Steinmann, and C. Corminboeuf, Int. J. Quantum Chem. **115**, 1265 (2015).
[63] A. D. Becke and E. R. Johnson, J. Chem. Phys. **122**, 154109 (2005).
[64] I. Chuang and G. Maciel, J. Phys. Chem. B **101**, 3052 (1997).
[65] C. T. Nguyen, B. Gu, T. Cheon, J. Park, M. R. Khan, S.-H. Kim, B. Shong, and H.-B.-R. Lee, Chem. Mater. **33**, 4435 (2021).
[66] B. Gu, N. T. Le, C. T. Nguyen, S. Yasmeen, H. Galji, Y. Kang, and H.-B.-R. Lee, Chem. Mater. **34**, 7635 (2022).
[67] See the supplementary material at https://www.scitation.org/doi/suppl/10.1116/6.0002153 for XRR fringe patterns and fitting results of discussed Ru metal films, oxygen XPS spectra, and XRD spectra with peak fitting results.